

Rarefied Gas Flow Simulation Based on Quasigasdynamic Equations

T. G. Elizarova, I. A. Graur, J. C. Lengrand,
A. Chpoun

Reprinted from

AIAA Journal

Volume 33, Number 12, Pages 2316–2324



A publication of the
American Institute of Aeronautics and Astronautics, Inc.
370 L'Enfant Promenade, SW
Washington, DC 20024-2518

Rarefied Gas Flow Simulation Based on Quasigasdynamic Equations

T. G. Elizarova* and I. A. Graur†

Russian Academy of Science, Moscow 125047, Russia
and

J. C. Lengrand‡ and A. Chpoun§

Centre National de la Recherche Scientifique, Meudon 92190, France

The treatment of rarefied gas flows by means of equations based on the mechanics of continuum media is desirable because solving such equations requires less computational resources than methods based on a molecular description. The present work aims at clarifying the domain of validity of two continuum approaches by comparing their results to a reference given by a direct simulation Monte Carlo method. The first continuum approach is based on the usual Navier–Stokes (NS) equations. The second one is based on the quasigasdynamic (QGD) equations that are derived from the Boltzmann equation. The present paper includes a self-consistent presentation of QGD equations. The flow along a flat plate has been considered for a freestream Mach number varying from 1.5 to 20 and a wall temperature taken successively equal to freestream and stagnation temperatures. The results suggest that the QGD equations are superior to the NS ones. A criterion is proposed for the validity of the continuum approaches.

Nomenclature

| | |
|---------------|------------------------------------|
| a | = speed of sound |
| d | = molecular diameter |
| E | = total energy |
| Kn | = Knudsen number, λ_1/L |
| L | = characteristic length |
| M | = Mach number |
| m | = molecular mass |
| Pr | = Prandtl number |
| p | = pressure |
| R | = perfect-gas constant |
| Re | = Reynolds number |
| T | = temperature |
| t | = time |
| u | = u' , velocity |
| (u, v) | = Cartesian velocity components |
| V | = $ u $, velocity |
| x_i | = (x, y) , Cartesian coordinates |
| γ | = specific heat ratio |
| ε | = internal energy |
| κ | = heat conductivity coefficient |
| λ | = mean free path |
| μ | = viscosity coefficient |
| ρ | = density |
| τ | = local characteristic time |

Subscripts

| | |
|---|-------------------------|
| 0 | = stagnation conditions |
| 1 | = freestream conditions |
| w | = wall conditions |

Received Dec. 22, 1994; revision received May 24, 1995; accepted for publication May 30, 1995. Copyright © 1995 by the American Institute of Aeronautics and Astronautics, Inc. All rights reserved.

*Leading Scientist, Institute for Mathematical Modelling, Miusskaya sq.4a.

†Research Scientist, Institute for Mathematical Modelling, Miusskaya sq.4a.

‡Leading Scientist, Laboratoire d'Aérothermique, 4 ter, route des gardes. Member AIAA.

§Assistant Professor, Laboratoire d'Aérothermique, 4 ter, route des gardes.

Introduction

THE treatment of rarefied gas flows by means of equations based on the mechanics of continuum media is desirable because solving such equations requires less computational resources than methods based on a molecular description, e.g., direct simulation Monte Carlo (DSMC).¹

A popular way of handling rarefied flow problems consists in solving Navier–Stokes (NS) equations with modified boundary conditions (BCs) to account for velocity slip and temperature jump.² Using Burnett equations is expected to lead to better results when the degree of nonequilibrium increases. Burnett equations, however, suffer from a number of disadvantages: they are considerably more complicated and there is no appropriate theory for writing their BCs. Furthermore, there is little evidence that they bring any significant improvement compared with NS equations for problems of practical interest. Both Burnett and NS equations can be considered as approximate models derived from Boltzmann equation using different orders of approximations.

In this paper, other continuum equations, i.e., quasigasdynamic (QGD) equations, are presented. QGD equations were originally constructed based on a kinetical model for the distribution function^{3,4} and were used successfully for creating robust numerical methods for viscous supersonic flows. Computational schemes obtained were called kinetical-consistent finite difference (KCFD) schemes.⁴ Now we consider the QGD system of equations as a specific mathematical model for gas flow simulation. The possibility of applying KCFD schemes based directly on a finite difference approximation of kinetical equations is considered in Ref. 5 for slightly rarefied gases.

A number of theoretical results have already been obtained in Ref. 6 for QGD equations. Particularly, the connection between QGD and NS was established. It was shown that for a stationary case, NS equations are the asymptotic limit of QGD equations for $\tau \rightarrow 0$, where τ is a characteristic collisional time. As should be done for any equation system that pretends to describe gasdynamic flows, the increase of the full thermodynamic entropy for QGD was demonstrated and the expression of the dissipation function was found.

Application of QGD equations to the shock-wave problem was discussed in Ref. 7, where results obtained for QGD model, NS model, kinetical model simulations, and some experimental data are compared. It was shown that QGD model describes the shock-wave structure in a wide range of Mach numbers. For low-Mach

numbers data obtained by NS, QGD, and kinetical models are just similar. As Mach number increases, the NS model loses its stability whereas QGD equations continue to provide gasdynamical profiles, although approximately.

In the present work a comparison between numerical solutions of QGD and NS equations is made for moderate Knudsen numbers, i.e., under conditions where the difference between the mentioned systems is not small. Results obtained with a DSMC method are used as reference data. Particular attention was paid to using consistent physical modeling in all approaches considered: monoatomic hard-sphere gas with full accommodation at the wall. Both QGD and NS equations can be derived from the Boltzmann equation, with the additional hypothesis of near-equilibrium distribution functions. The DSMC method can be regarded either as a numerical experiment at a molecular level or as a numerical solution of the Boltzmann equation. Therefore, the DSMC method is based on less restrictive hypotheses, which justifies using it as a reference for a given physical modeling.

The test problem retained is the flow along a semi-infinite sharp flat plane parallel to the freestream. A systematic study was carried out by varying freestream Mach number and wall temperature.

Because the problem considered does not introduce any length scale except the freestream mean free path, the abscissa along the plate is directly related to any parameter that characterizes the degree of flow rarefaction: Reynolds number, rarefaction parameter, interaction parameter, Knudsen number, etc. In other words, considering different abscissas along the plate is equivalent to considering different rarefaction levels.

The objective of the work reported herein was to examine whether QGD equations brought some improvement compared with NS equations for the treatment of rarefied flows. More specifically, the objective was to define a criterion for the validity of QGD and NS sets of equations by comparing these results with those obtained using a DSMC method.

QGD Model

Short Presentation of QGD Equations

QGD equations can be obtained by averaging over molecular velocities a kinetical equation in the form

$$f_t + (\xi \nabla) f - (\xi \nabla) \tau (\xi \nabla) f = \mathcal{J}(f, f') \quad (1)$$

where $f = f(x, \xi, t)$ is the one-particle distribution function of molecular velocities ξ at point x , and τ is a local characteristic time. The right-hand side term is a modified Boltzmann collision integral.

In this paper we will not present in detail how Eq. (1) was obtained. An equation such as Eq. (1) was first constructed in Ref. 3 by describing the molecular motion as a cyclic process of free flight and instantaneous Maxwellization. For the phase of collisionless moving, the distribution function was expanded into a Taylor series for the parameter $\xi \tau$. In this approach, the diffusive-like term in Eq. (1) arose as a result of usual gradient expansion for space derivatives. In Ref. 8, based on a simple physical model, it appears as being extracted from the usual Boltzmann collision integral using an expansion in the small parameter τ .

Equation (1) allows one to derive macroscopic QGD equations that include viscosity and heat transfer even when the closure of the system is based on the equilibrium distribution function instead of a special NS expression for f . Dissipative terms in QGD equations appear when averaging the relaxation term in the form $(\xi \nabla) \tau (\xi \nabla) f$. Transport phenomena appear in the equations through time τ . The condition

$$\tau = \mu / p \quad (2)$$

ensures the consistency with the actual gas viscosity used in NS equations. For variable hard sphere (VHS) molecules, it was shown in Ref. 9 that τ is related to the molecular collision frequency ν by $\tau = 30 / [\nu(7 - 2\omega)(5 - 2\omega)]$ where ω is the exponent of the viscosity-temperature relationship. For hard sphere molecules $\tau = 5 / (4\nu)$.

With usual notations, the QGD system becomes

$$\rho_t + \nabla_i \rho u^i = \nabla_i (\mu / p) (\nabla_j \rho u^i u^j + \nabla^i p) \quad (3)$$

$$(\rho u^k)_t + \nabla_i \rho u^i u^k + \nabla^k p = \nabla_i (\mu / p) \nabla_j \rho u^i u^j u^k + \nabla_i (\mu / p) \nabla^i p u^k + \nabla_i (\mu / p) \nabla^k p u^i + \nabla^k (\mu / p) \nabla_i p u^i \quad (4)$$

$$E_t + \nabla_i (E + p) u^i = \nabla_i \frac{\mu}{p} \nabla_j (E + 2p) u^i u^j + \nabla_i \frac{\mu}{p} \nabla^i \frac{p u^k u_k}{2} + \frac{\gamma}{\gamma - 1} \nabla_i \frac{\mu}{\rho} \nabla^i p + \frac{\gamma P r^{-1}}{\gamma - 1} \nabla_i \mu \nabla^i \frac{p}{\rho} \quad (5)$$

For a perfect gas, the system is completed by

$$E = \rho (u^i u_i / 2 + \varepsilon), \quad \varepsilon = p / (\gamma - 1), \quad p = \rho R T \quad (6)$$

Adding, finally, the initial and boundary conditions, we obtain a closed system of equations that describes the space-time evolution of the macroscopic parameters of the gas: velocity, density, pressure, and total energy. The last term in the energy equation is the heat flux equal to $\nabla_i \kappa \nabla^i T$.

The system of equations (3–5) can be nondimensionalized through freestream scaling quantities: $\rho_1, a_1 = \sqrt{(\gamma R T_1)}, \mu_1$, and a characteristic scale length L . As in the NS equations, the factor M_1 / Re_1 appears in the right-hand side of all equations, where $M_1 = V_1 / a_1$, and $Re_1 = V_1 L \rho_1 / \mu(T_1)$.

The nondimensional QGD system in two-dimensional flow is

$$\begin{aligned} \frac{\partial \rho}{\partial t} + \frac{\partial \rho u}{\partial x} + \frac{\partial \rho v}{\partial y} &= \frac{M_1}{Re_1} \left[\frac{\partial}{\partial x} \left(\frac{\mu}{p} \frac{\partial}{\partial x} (\rho u^2 + p) \right) \right. \\ &+ \frac{\partial}{\partial y} \left(\frac{\mu}{p} \frac{\partial}{\partial y} (\rho v^2 + p) \right) + \frac{\partial}{\partial x} \left(\frac{\mu}{p} \frac{\partial}{\partial y} \rho u v \right) \\ &\left. + \frac{\partial}{\partial y} \left(\frac{\mu}{p} \frac{\partial}{\partial x} \rho u v \right) \right] \quad (7) \end{aligned}$$

$$\begin{aligned} \frac{\partial \rho u}{\partial t} + \frac{\partial}{\partial x} (\rho u^2 + p) + \frac{\partial \rho u v}{\partial y} &= \frac{M_1}{Re_1} \left[\frac{\partial}{\partial x} \left(\frac{\mu}{p} \frac{\partial}{\partial x} (\rho u^3 + 3 p u) \right) \right. \\ &+ \frac{\partial}{\partial y} \left(\frac{\mu}{p} \frac{\partial}{\partial y} (\rho u v^2 + p u) \right) + \frac{\partial}{\partial x} \left(\frac{\mu}{p} \frac{\partial}{\partial y} \rho u^2 v \right) \\ &\left. + \frac{\partial}{\partial y} \left(\frac{\mu}{p} \frac{\partial}{\partial x} \rho u^2 v \right) + \frac{\partial}{\partial x} \left(\frac{\mu}{p} \frac{\partial}{\partial y} p v \right) + \frac{\partial}{\partial y} \left(\frac{\mu}{p} \frac{\partial}{\partial x} p v \right) \right] \quad (8) \end{aligned}$$

$$\begin{aligned} \frac{\partial \rho v}{\partial t} + \frac{\partial}{\partial y} (\rho v^2 + p) + \frac{\partial \rho u v}{\partial x} &= \frac{M_1}{Re_1} \left[\frac{\partial}{\partial y} \left(\frac{\mu}{p} \frac{\partial}{\partial y} (\rho v^3 + 3 p v) \right) \right. \\ &+ \frac{\partial}{\partial x} \left(\frac{\mu}{p} \frac{\partial}{\partial x} (\rho v u^2 + p v) \right) + \frac{\partial}{\partial x} \left(\frac{\mu}{p} \frac{\partial}{\partial y} \rho u v^2 \right) \\ &\left. + \frac{\partial}{\partial y} \left(\frac{\mu}{p} \frac{\partial}{\partial x} \rho u v^2 \right) + \frac{\partial}{\partial x} \left(\frac{\mu}{p} \frac{\partial}{\partial y} p u \right) + \frac{\partial}{\partial y} \left(\frac{\mu}{p} \frac{\partial}{\partial x} p u \right) \right] \quad (9) \end{aligned}$$

$$\begin{aligned}
\frac{\partial E}{\partial t} + \frac{\partial}{\partial x} u(E+p) + \frac{\partial}{\partial y} v(E+p) &= \frac{M_1}{Re_1} \\
&\times \left[\frac{\partial}{\partial x} \left(\frac{\mu}{\rho} \frac{\partial}{\partial x} u^2(E+2.5p) \right) + \frac{\partial}{\partial y} \left(\frac{\mu}{\rho} \frac{\partial}{\partial y} v^2(E+2.5p) \right) \right] \\
&+ \frac{\partial}{\partial x} \left(\frac{\mu}{2\rho} \frac{\partial}{\partial x} v^2 p \right) + \frac{\partial}{\partial y} \left(\frac{\mu}{2\rho} \frac{\partial}{\partial y} u^2 p \right) \\
&+ \frac{\partial}{\partial x} \left(\frac{\mu}{\rho} \frac{\partial}{\partial y} uv(E+2p) \right) + \frac{\partial}{\partial y} \left(\frac{\mu}{\rho} \frac{\partial}{\partial x} uv(E+2p) \right) \\
&+ \frac{\gamma}{\gamma-1} \left(\frac{\partial}{\partial x} \left(\frac{\mu}{\rho} \frac{\partial p}{\partial x} \right) + \frac{\partial}{\partial y} \left(\frac{\mu}{\rho} \frac{\partial p}{\partial y} \right) \right) \\
&+ \frac{\gamma Pr^{-1}}{\gamma-1} \left(\frac{\partial}{\partial x} \left(\mu \frac{\partial p}{\partial x} \rho \right) + \frac{\partial}{\partial y} \left(\mu \frac{\partial p}{\partial y} \rho \right) \right) \quad (10)
\end{aligned}$$

QGD equations differ from NS equations by the structure of the dissipative terms in the right-hand side of the momentum and energy equations and by the presence of a divergence term in the right-hand side of the continuity equation. The numerical work that will be presented later confirms that QGD and NS results coincide for small values of Kn , the former being closer to the reference DSMC results for moderate values of Kn .

Wall Boundary Conditions for QGD System

The continuity equation in the QGD system has additional space derivatives of higher order than the corresponding NS equation. This is the reason why it requires an additional boundary condition. The latter is obtained by equating the normal mass flow in NS and QGD formulations. For NS equations, the no-flow condition through the solid boundary is satisfied if $u_n = 0$, where u_n is the normal velocity. For a plane wall, QGD equations require additionally that

$$\frac{\partial p}{\partial n} = 0 \quad (11)$$

This condition is classical in the boundary-layer approximation. The boundary condition given by Eq. (11) together with the condition $u_n = 0$ results in QGD and NS models presenting the same expressions for the exchange of energy and tangential momentum with the wall,

$$q = \mu u_t \frac{\partial u_t}{\partial n} + \kappa \frac{\partial T}{\partial n} \quad (12)$$

$$\sigma^{xy} = \mu \frac{\partial u_t}{\partial n} \quad (13)$$

where u_t is the tangential velocity component. To close the system of equations, boundary conditions for tangential velocity and wall temperature (or heat flux) are necessary. These BCs for the QGD system are the same as for the NS one. No-slip BCs are written as

$$u_t = 0, \quad T = T_w \quad \text{or} \quad \kappa \frac{\partial T}{\partial n} = q_w$$

Conditions that account for velocity slip and temperature jump can be found in Ref. 10:

$$u_s = \left(\frac{\sqrt{\pi} \mu}{\rho \sqrt{2RT}} \frac{\partial u}{\partial y} \right)_s \quad (14)$$

$$v_s = 0 \quad (15)$$

$$T_s - T_w = \frac{\sqrt{\pi}}{2R} \left(\frac{1}{\sqrt{2RT}} \frac{\kappa}{\rho} \frac{\partial T}{\partial y} \right)_s \quad (16)$$

Another variant, taken from Ref. 2, has also been used for the present problem, bringing negligible differences in the results.

Peculiarities of Numerical Methods for QGD Equations

The structure of the dissipation terms makes stability properties better for QGD equations than for NS formulation. This was

demonstrated by carrying out NS and QGD calculations for the problem considered here. For $M_1 = 1.5, 2,$ and 5 and $T_w = T_0$, the same scheme (explicit centered scheme, with no added dissipation) was used, with the same grids and time steps. For $M_1 = 1.5$ and $M_1 = 2$ convergence was virtually identical, but for $M_1 = 5$ convergence was reached for QGD and not for NS equations.

Moreover, the form of QGD equations suggests a simple and efficient numerical algorithm to overcome the problem of oscillations that appear when computing flows at large Reynolds numbers using methods of high-order accuracy. Usually this problem is overcome by smoothing the numerical solution in the regions of large gradients or by using a shock-fitted boundary. In shock-capturing methods, artificial dissipation is introduced into the gasdynamic finite difference equations, or the scheme accuracy is decreased in the shock-wave region [flux-vector-splitting methods of Steger and Warming type, total variation diminishing methods, etc.].

The problem of numerical instabilities in the QGD system is solved in the following manner. For convenience μ is written as $\bar{\mu}$ in some of the dissipation terms,

$$\begin{aligned}
\frac{\partial \rho}{\partial t} + \frac{\partial \rho u}{\partial x} + \frac{\partial \rho v}{\partial y} &= \frac{\partial}{\partial x} \left(\frac{\bar{\mu}}{\rho} \frac{\partial}{\partial x} (\rho u^2 + p) \right) \\
&+ \frac{\partial}{\partial y} \left(\frac{\bar{\mu}}{\rho} \frac{\partial}{\partial y} (\rho v^2 + p) \right) + \frac{\partial}{\partial x} \left(\frac{\mu}{\rho} \frac{\partial}{\partial y} \rho uv \right) \\
&+ \frac{\partial}{\partial y} \left(\frac{\mu}{\rho} \frac{\partial}{\partial x} \rho uv \right) \quad (17)
\end{aligned}$$

$$\begin{aligned}
\frac{\partial \rho u}{\partial t} + \frac{\partial}{\partial x} (\rho u^2 + p) + \frac{\partial \rho uv}{\partial y} &= \frac{\partial}{\partial x} \left(\frac{\bar{\mu}}{\rho} \frac{\partial}{\partial x} (\rho u^3 + 3pu) \right) \\
&+ \frac{\partial}{\partial y} \left(\frac{\bar{\mu}}{\rho} \frac{\partial}{\partial y} \rho uv^2 \right) + \frac{\partial}{\partial y} \left(\frac{\bar{\mu}}{\rho} u \frac{\partial p}{\partial y} \right) + \frac{\partial}{\partial y} \left(\mu \frac{\partial u}{\partial y} \right) \\
&+ \frac{\partial}{\partial x} \left(\frac{\mu}{\rho} \frac{\partial}{\partial y} \rho u^2 v \right) + \frac{\partial}{\partial y} \left(\frac{\mu}{\rho} \frac{\partial}{\partial x} \rho u^2 v \right) + \frac{\partial}{\partial x} \left(\frac{\mu}{\rho} \frac{\partial}{\partial y} p v \right) \\
&+ \frac{\partial}{\partial y} \left(\frac{\mu}{\rho} \frac{\partial}{\partial x} p v \right) \quad (18)
\end{aligned}$$

$$\begin{aligned}
\frac{\partial \rho v}{\partial t} + \frac{\partial}{\partial y} (\rho v^2 + p) + \frac{\partial \rho uv}{\partial x} &= \frac{\partial}{\partial y} \left(\frac{\bar{\mu}}{\rho} \frac{\partial}{\partial y} (\rho v^3 + 3pv) \right) \\
&+ \frac{\partial}{\partial x} \left(\frac{\bar{\mu}}{\rho} \frac{\partial}{\partial x} \rho v u^2 \right) + \frac{\partial}{\partial x} \left(\frac{\bar{\mu}}{\rho} v \frac{\partial p}{\partial x} \right) + \frac{\partial}{\partial x} \left(\mu \frac{\partial v}{\partial x} \right) \\
&+ \frac{\partial}{\partial x} \left(\frac{\mu}{\rho} \frac{\partial}{\partial y} \rho uv^2 \right) + \frac{\partial}{\partial y} \left(\frac{\mu}{\rho} \frac{\partial}{\partial x} \rho uv^2 \right) + \frac{\partial}{\partial x} \left(\frac{\mu}{\rho} \frac{\partial}{\partial y} p u \right) \\
&+ \frac{\partial}{\partial y} \left(\frac{\mu}{\rho} \frac{\partial}{\partial x} p u \right) \quad (19)
\end{aligned}$$

$$\begin{aligned}
\frac{\partial E}{\partial t} + \frac{\partial}{\partial x} u(E+p) + \frac{\partial}{\partial y} v(E+p) \\
&= \frac{\partial}{\partial x} \left(\frac{\bar{\mu}}{\rho} \frac{\partial}{\partial x} u^2(E+2.5p) \right) + \frac{\partial}{\partial y} \left(\frac{\bar{\mu}}{\rho} \frac{\partial}{\partial y} v^2(E+2.5p) \right) \\
&+ \frac{\partial}{\partial x} \left(\frac{\bar{\mu}}{2\rho} v^2 \frac{\partial p}{\partial x} \right) + \frac{\partial}{\partial x} \left(\mu \frac{\partial}{\partial x} \frac{v^2}{2} \right) + \frac{\partial}{\partial y} \left(\frac{\bar{\mu}}{2\rho} u^2 \frac{\partial p}{\partial y} \right) \\
&+ \frac{\partial}{\partial y} \left(\mu \frac{\partial}{\partial y} \frac{u^2}{2} \right) + \frac{\partial}{\partial x} \left(\frac{\mu}{\rho} \frac{\partial}{\partial y} uv(E+2p) \right) \\
&+ \frac{\partial}{\partial y} \left(\frac{\mu}{\rho} \frac{\partial}{\partial x} uv(E+2p) \right) + \frac{\gamma}{\gamma-1} \left[\frac{\partial}{\partial x} \left(\frac{\bar{\mu}}{\rho} \frac{\partial p}{\partial x} \right) \right. \\
&\left. + \frac{\partial}{\partial y} \left(\frac{\bar{\mu}}{\rho} \frac{\partial p}{\partial y} \right) \right] + \frac{\gamma Pr^{-1}}{\gamma-1} \left[\frac{\partial}{\partial x} \mu \frac{\partial p}{\partial x} \rho + \frac{\partial}{\partial y} \mu \frac{\partial p}{\partial y} \rho \right] \quad (20)
\end{aligned}$$

The terms describing viscosity and heat conductivity of NS type and having the order of 1 [$\mathcal{O}(1)$] in the boundary-layer (Prandtl)

Table 1 Flow parameters

| Mach number, M_1 | 1.5 | 2 | 5 | 10 | 20 |
|---|-------|-------|-------|--------|-------|
| Reynolds number, $Re_1 = \rho_1 V_1 L / \mu(T_1)$ | 247.2 | 329.6 | 824.1 | 1648.1 | 3296 |
| $M_1 / \sqrt{Re_1}$ | 0.095 | 0.110 | 0.174 | 0.246 | 0.348 |
| Reynolds number ^a $Re_w = \rho_1 V_1 L / \mu(T_w)$ | 186.9 | 215.8 | 269.7 | 281.3 | 284.4 |

^a Re_w calculated for $T_w = T_0$; note that $Re_w = Re_1$ if $T_w = T_1$.

approximation have been isolated and kept unchanged. The mixed space gradients have been also unchanged.

A second-order space approximation for the system (17–20) is applied to get the corresponding finite difference equations. When writing these equations, $\tilde{\mu}$ is expressed as $\mu + \beta \rho h a$, where h denotes the grid step in the x or y direction at the current location and β ($0 \leq \beta \leq 1$) is the smallest possible parameter that ensures solution stability. This is equivalent to considering a viscosity $\mu' \propto \rho h a$, in addition to the real viscosity $\mu \propto \rho \lambda a$ in some terms. The space accuracy of the resulting scheme, thus, becomes $\mathcal{O}(h^2 + \beta h)$. The system of equations (17–20) has been used in the present work for numerical simulation at large Mach numbers.

The expression of $\tilde{\mu}$ is derived from the artificial viscosity introduced in the so-called KCFD schemes with correction.⁴ KCFD schemes have been used in the case $\lambda \ll h$ and $\beta = 1/2$ for the numerical simulation of gas flows at large Reynolds numbers.

Although NS equations do not include the terms that have been affected by the foregoing procedure, the latter could be introduced artificially into the NS dissipation terms for stability purpose. The same scheme can, thus, be used for viscous flow (viscosity μ), for inviscid flows (artificial viscosity) in some terms, and for flows exhibiting both viscous and inviscid regions (with local values of β).

Computational Work

Flow Conditions

The test problem retained for the present work was flow along a semi-infinite sharp flat plate parallel to the freestream velocity. A systematic study was carried out by varying the freestream Mach number M_1 from 1.5 to 20 and setting the wall temperature T_w equal successively to the freestream temperature T_1 and to the freestream stagnation temperature T_0 .

The gas was monoatomic ($\gamma = 5/3$, $Pr = 2/3$). In QGD and NS calculations, the viscosity law ($\mu \propto \sqrt{T}$) was chosen to be consistent with the hard sphere molecular model used in DSMC calculations.¹¹

$$\mu = \frac{5m}{16d^2} \sqrt{\frac{RT}{\pi}}$$

The three numerical methods were also consistent in modeling the gas/surface interaction: diffuse reflection with perfect accommodation at T_w was assumed.

QGD calculations were performed on dimensionless quantities, whereas NS and DSMC calculations used dimensional quantities. In the results presented here, the flow parameters have been nondimensionalized by their freestream values, and the lengths have been nondimensionalized by the freestream mean free path λ_1 . Based on Ref. 11,

$$\lambda = 16 \mu / (5 \rho \sqrt{2\pi RT})$$

Although the problem considered is a semi-infinite flat plate, practical calculations were carried out for a plate length of approximately $100 \lambda_1$. This covered the Knudsen number range 0.01 and larger.

Table 1 presents a number of parameters relative to the different flow conditions. The reference length L used in Re_1 is equal to $100 \lambda_1$. Table 1 includes the values of a Reynolds number Re_w based on wall temperature rather than on freestream temperature. Re_w was found¹² to be a better correlation parameter than Re_1 .

QGD Calculations

QGD calculations were carried out, based on the equations and on the numerical procedure described earlier. A finite difference scheme was constructed based on the dimensionless form of

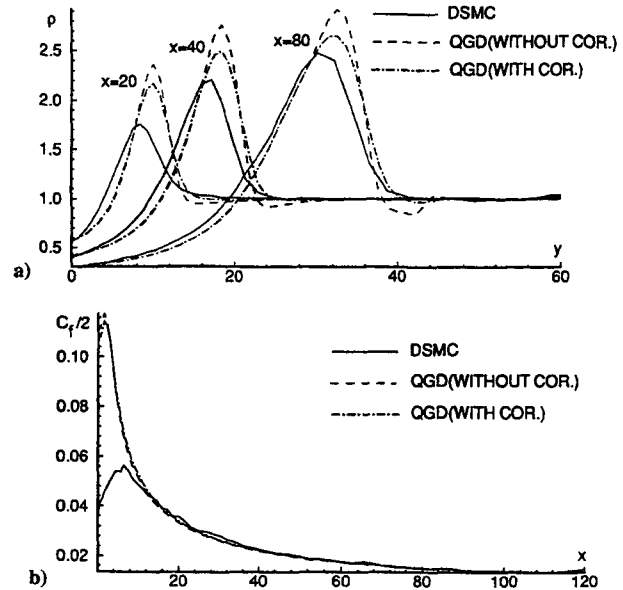


Fig. 1 Correction procedure for QGD equations; $M_1 = 10$, $T_w = T_0$, x denotes reciprocal Kn : a) density profiles and b) $C_f/2$ distributions.

Eqs. (7–10). The code uses a finite volume approach with a centered approximation for all space derivatives, including the convective terms. The flow parameters are calculated in the nodes of the computational grid, and the fluxes are calculated in the centered points between the nodes. The symmetry plane and the plate surface are placed in the centered points. The steady-state solution is obtained as a limit of a time-evolving process. The time step is chosen from the Courant stability condition $\Delta t = \alpha \min(h/V)$, where $V = a + \sqrt{u^2 + v^2}$ and $h = \min(\delta x, \delta y)$. Coefficient α was chosen experimentally in the range 0.01–0.1. The computation was stopped when the steady-state solution was achieved, based on the following convergence criterion: $\rho(t + \Delta t) - \rho(t) / \Delta t \leq 0.001$, where the difference is averaged over all grid points.

The numerical method used in the present work is probably not the most efficient one, but the objective was to examine the validity domain of QGD equations rather than optimizing their numerical solution. Applying efficient methods developed for NS equations should enable one to solve QGD equations more efficiently.

To check grid convergence, results were obtained at $M_1 = 5$ with two values of h and are presented in Ref. 9. The fine grid calculation was limited to a smaller domain. Agreement between the two calculations is excellent. The main discrepancy occurs near the downstream boundary of the domain (thus indicating the extent of its zone of influence). The differences that are visible on the isodensity lines appear in a region of weak gradients, where the position of the isolines is very sensitive to small variations in the function to be plotted. A similar grid sensitivity study was carried out for $M_1 = 2$ with both wall temperature assumptions and resulted in differences only at large abscissas and at large distances from the plate, where the cell size was the largest one.

In the present QGD calculations (without the correction procedure), the onset of fluctuations is visible on density profiles in the shock region for $M_1 = 10$ and $T_w = T_0$, and computations at $M_1 = 20$ failed. The latter case was treated using the same finite difference scheme applied to Eqs. (17–20) with a correction procedure ($\beta = 0.15$ for $T_w = T_0$, $\beta = 0.1$ for $T_w = T_1$). The consequence of the correction procedure is demonstrated in Fig. 1a, where the density

distributions at $x = 20, 40,$ and 80 for $M = 10, T_w = T_0$ for $\beta = 0$ (without correction) and $\beta = 0.1$ (with correction) are plotted. The solution without correction has an instability shown by the local minimum in density profile at $x = 40$ and $x = 80$. The correction leads to a small smoothing of a density profile and removes completely the corresponding numerical instability. All gasdynamic values outside the mentioned region are just the same in this case, and the correction does not affect the parameters at the wall (Fig. 1b). For comparison, the corresponding DSMC solution is also shown.

DSMC and NS Calculations

DSMC calculations were carried out for the tests cases presented before. The computer code direct simulation of rarefied gas flows (DISIRAF) had been developed at the Laboratoire d'Aérothermique du CNRS and has been applied to a variety of applications as described in Refs. 12 and 13. This code is based on the DSMC method of Bird.¹ The molecular interaction model was the VHS model used here in the particular case of hard sphere molecules. Although the code allows for mixtures of polyatomic molecules, it was used here for a pure monoatomic gas. The correct molecular frequency was ensured by using the no time counter algorithm.

The number of real molecules simulated by a computational molecule (the weighting factor of the molecule) was variable. In a given cell, it was taken equal to $(n_{\text{approx}} V_{\text{cell}})/10$, where n_{approx} was an estimation of the local number density and V_{cell} the volume of the cell. For an initial calculation, n_{approx} was taken equal to n_1 . This resulted in a cell population that ranged from a few molecules to tens of molecules. The number density resulting from the initial solution was then used as a better estimate of n to readjust the weight of the molecules. Then a new calculation was launched. The number of molecules per cell was found to be nearly constant (9–11), and the results were retained.

Molecules were injected through the upstream, downstream, and lateral boundaries with distribution functions corresponding to freestream parameters. The plate ($y = 0, 0 < x < x_{\text{max}}$) was considered as a diffusely reflecting surface with perfect accommodation at wall temperature T_w . The plane ($y = 0, x_{\text{min}} < x < 0$) was considered as a specularly reflecting surface. For high values of M_1 , the inward flow rate of molecules through the downstream boundary is negligibly small and can indifferently be set or removed. At $M_1 = 20$, however, it was found necessary to remove the inflow downstream boundary condition to avoid underflows.

Most calculations required a maximum of 3 megabytes of memory. Approximately $20\text{--}25 \times 10^6$ molecular collisions were calculated in 1 h of CPU time on a IBM 3090 computer.

The time step δt was sufficiently small to ensure $v \times \delta t < 1$ in each cell, where v is the collision frequency of a molecule, estimated from the local macroscopic flow parameters¹¹:

$$v = 4n d^2 \times \sqrt{\pi k T/m}$$

for hard sphere molecules ($\omega = 1/2$).

Calculations were first performed for the near-adiabatic case $T_w = T_0$. Different grids were used to check the sensitivity of the results to the grid parameters and to adjust the computational domain to the extent of the region disturbed by the presence of the plate. Test cases corresponding to $M_1 = 1.5, 2, 5,$ and 10 were treated using an initial grid and no downstream injection. Then calculations for $M_1 = 1.5$ were repeated with a grid that covered a larger domain and was associated with downstream injection. Comparing the results gave an indication of the region that is affected by the downstream boundary conditions and the extent of the computational domain. The results retained for $M_1 = 1.5$ are unaffected by the downstream boundary condition for $x < 90$. Calculations required 97 min of CPU time. Data sampling began when steady state was achieved. This time was considered to be reached when the number of molecules in the computational domain became nearly constant ($t \approx 7.5 \times$ the aerodynamic time x_{max}/V_1). For the computation, 45% of the computational time was used to reach steady state and 55% to gather statistical information.

In the same way, calculations for the near-adiabatic cases at $M_1 = 2, 5,$ and 10 were repeated and found unaffected by the downstream boundary condition up to $x = 90$.

To check for a possible influence of space discretization, the near-adiabatic test case at $M_1 = 10$ was recalculated with a grid C that differs from the previous one D by a smaller extent in the x and y direction and by cell dimensions (δx_{min} and δy_{min}) smaller by a factor of 2. The results exhibit no difference, except for the influence of the downstream boundary that occurs for a smaller value of x , due to the smaller value of x_{max} (see Ref. 9). The same grid was used for the cold-wall test cases.

For comparison, the same test cases were also calculated with NS equations using a commercial code¹⁴ (INCA). The code used a finite volume upwind implicit method with flux-vector splitting of Steger and Warming. The diffusion terms were evaluated using centered differences. Velocity slip and temperature jump were used as boundary conditions along the wall, in the form of Eqs. (14–16). Space discretization was characterized by cell dimensions $\delta x_{\text{min}} = \delta y_{\text{min}} = 0.2$ and a number of cells equal to 4000 for a typical calculation. These values were based on a grid sensitivity study that was conducted for another work.¹⁵

Discussion

The distributions of wall quantities [p and $C_f/2 = \sigma^{xy}/(\rho_1 V_1^2)$] for $M_1 = 2, 5, 10,$ and 20 are given in Figs. 2–5 for $T_w = T_0$

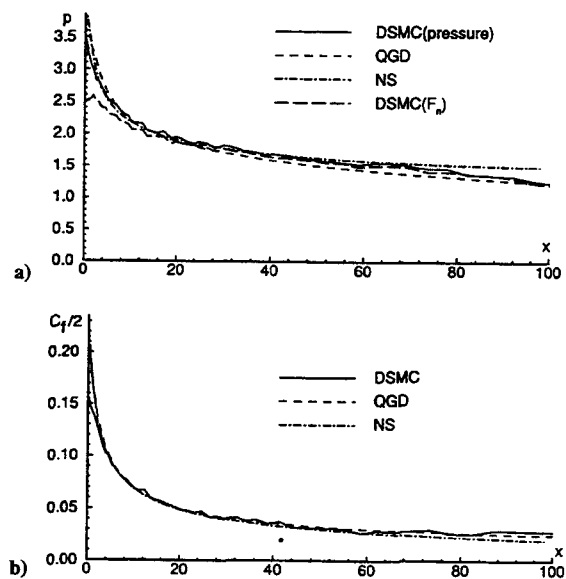


Fig. 2 $M_1 = 2$ and $T_w = T_0$: a) normal stress and pressure and b) $C_f/2$.

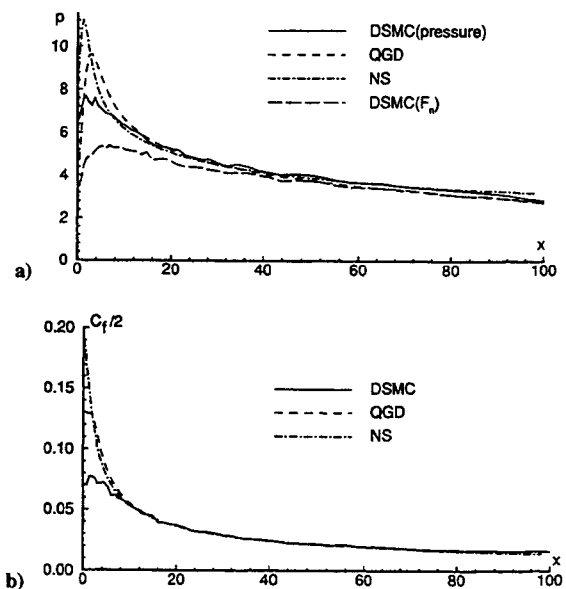


Fig. 3 $M_1 = 5$ and $T_w = T_0$: a) normal stress and pressure and b) $C_f/2$.

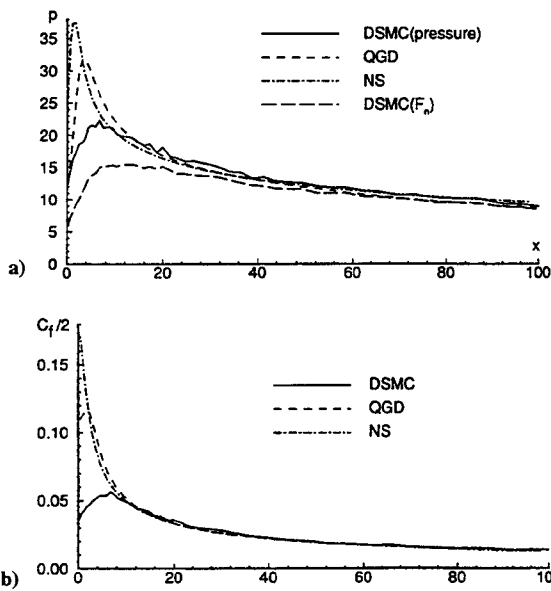


Fig. 4 $M_1 = 10$ and $T_w = T_0$: a) normal stress and pressure and b) $C_f/2$.

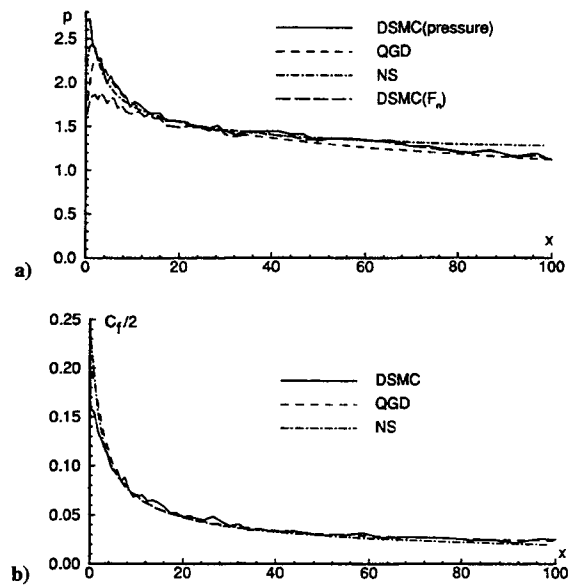


Fig. 6 $M_1 = 2$ and $T_w = T_1$: a) normal stress and pressure and b) $C_f/2$.

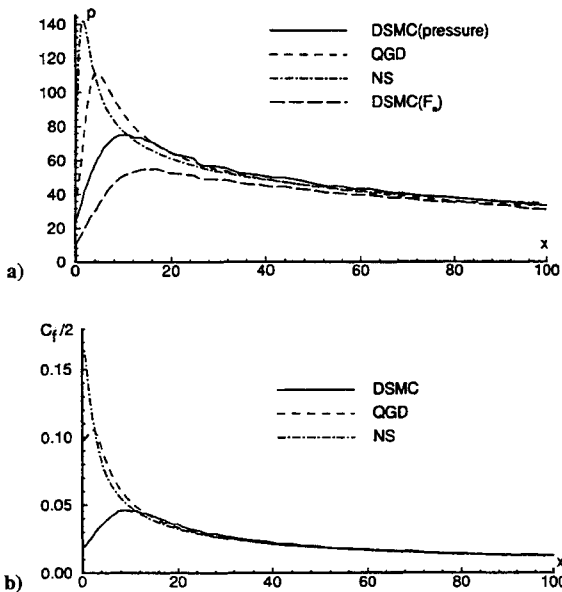


Fig. 5 $M_1 = 20$ and $T_w = T_0$: a) normal stress and pressure and b) $C_f/2$.

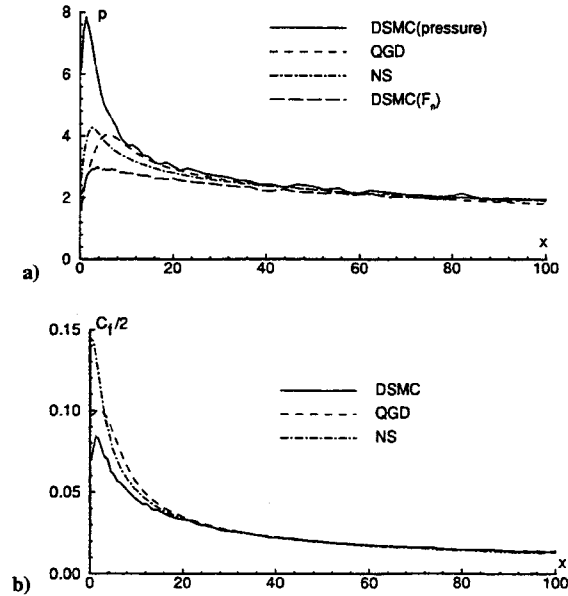


Fig. 7 $M_1 = 5$ and $T_w = T_1$: a) normal stress and pressure and b) $C_f/2$.

and in Figs. 6–9 for $T_w = T_1$. The distribution of Stanton number $St = C_h = q/[\rho_1 V_1 C_p (T_0 - T_w)]$ is not presented here because it was found to be very close to that of $C_f/2$. This is consistent with the Reynolds' analogy: $C_h \approx Pr^{-2/3} C_f/2$ in the boundary-layer theory and $C_h = C_f/2$ in the free molecular regime for $T_w = T_1$.

The profiles of flow parameters ρ and p against y at abscissas $x = 10, 40,$ and 80 for $M_1 = 2, 10,$ and 20 are plotted in Figs. 10–12 for $T_w = T_0$ and in Figs. 13–15 for $T_w = T_1$. For more details concerning the numerical results, see Ref. 9.

Consistent with the fact that NS equations are the asymptotic limit of QGD equations for $Kn \rightarrow 0$ (see Ref. 6), it is expected that QGD and NS results tend to coincide for large values of x . This observation is clear on the distributions of most wall quantities and can be made on flowfield profiles (e.g., Figs. 11 and 14 for $M_1 = 10$). However, the profiles at $x = 80$ in Figs. 10 and 13 ($M_1 = 2$) are affected by an excessively large space step used in QGD equations far from the plate. Also, the comparison between NS and QGD results in Figs. 12 and 15 ($M_1 = 20$) is affected by the differences in the techniques for artificial dissipation.

Pressure profiles perpendicular to the plate for $M_1 = 2, 10,$ and 20 at both wall temperatures have been plotted in Figs. 10b–15b to

determine whether the additional BC $\partial p/\partial n$ is restrictive compared with NS equations, where this condition is not prescribed. Far from the leading edge, NS results exhibit actually a zero pressure gradient at the wall, even for the cold wall. Close to the leading edge, NS and QGD profiles exhibit nearly identical nonzero pressure gradients. Thus, the additional BC in QGD affects the solution only at a few nearest wall grid points. DSMC results also exhibit zero pressure gradients for the hot wall (Figs. 10b–12b) except near the leading edge ($x = 10$) and large pressure gradients for large values of M_1 in the cold wall cases (Figs. 14b–15b). These gradients, however, affect only the Knudsen layer that is not claimed to be described exactly by the continuum approach. Slip BCs just account for the influence of the Knudsen layer on the rest of the flowfield.

For small Mach numbers both continuum models come to close agreement rapidly with DSMC. The region near the trailing edge, however, is affected by the differences in formulating the downstream boundary conditions. The BC upstream influence is particularly important in NS calculations for small Mach numbers (Figs. 2a and 6a).

As M_1 increases, discrepancies appear near the leading edge of the plate (Figs. 2b–9b). Both these discrepancies and the extent of

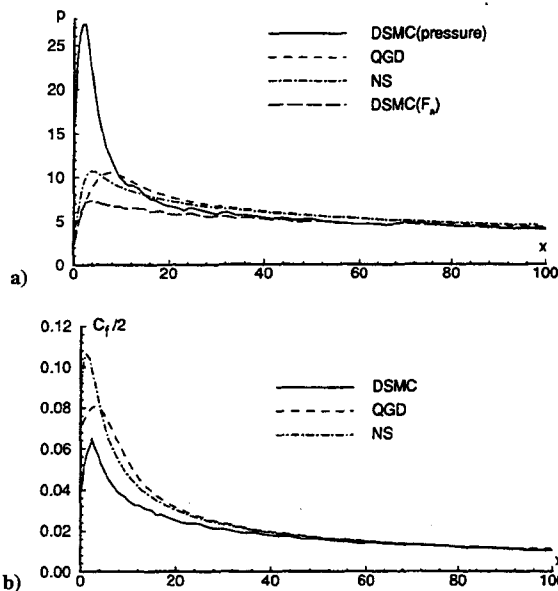


Fig. 8 $M_1 = 10$ and $T_w = T_1$: a) normal stress and pressure and b) $C_f/2$.

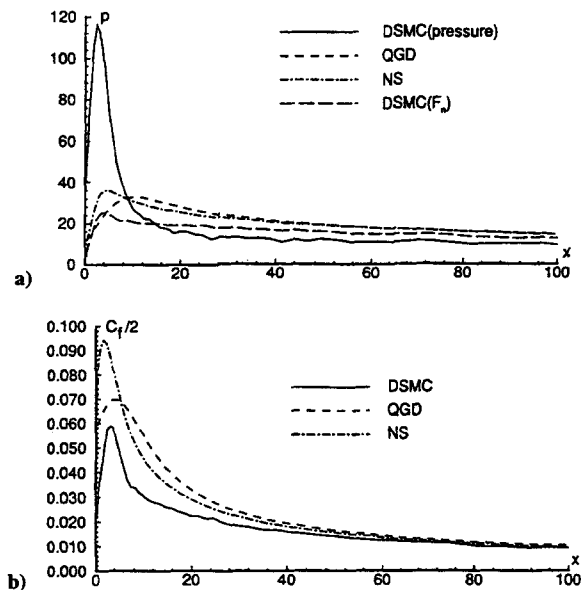


Fig. 9 $M_1 = 20$ and $T_w = T_1$: a) normal stress and pressure and b) $C_f/2$.

the region where they appear increase with increasing M_1 . QGD results are generally closer to DSMC than NS results. Thus, QGD equations can be considered an improvement, when compared with the NS equations in the domain of large Mach numbers in the slip-flow regime. This is due to the expression of dissipation in the QGD model. The ratio of QGD additional terms to the NS dissipation terms in the momentum equation is proportional to V^2 . Thus, the difference between QGD and NS increases with M_1 .

Both continuum models, however, depart from DSMC at approximately the same abscissa x (considered here as a dimensional quantity). This abscissa x was introduced into the expressions of a number of parameters that can be used to characterize the rarefaction level and that are presented hereafter. $Kn_x = \lambda_1/x$ and $Re_x = \rho_1 V_1 x / \mu(T_1)$ are the Knudsen and Reynolds numbers based on length x . $\bar{V}_x = M_1 \sqrt{C/Re_x}$ is a classical rarefaction parameter where $C = [\mu(T_r)/\mu(T_1)] / (T_r/T_1)$ is the Chapman-Rubensin constant, and $T_r = T_1 + 0.54(T_w - T_1) + 0.16\sqrt{Pr}(\gamma - 1)M_1^2/2$ is Monaghan's reference temperature. The parameter $\chi_x = \bar{V}_x M_1^2$ characterizes shock-wave/boundary-layer interaction. $M_1/\sqrt{Re_x}$ was also considered. $Re_{w,x} = \rho_1 V_1 x / \mu(T_w)$,

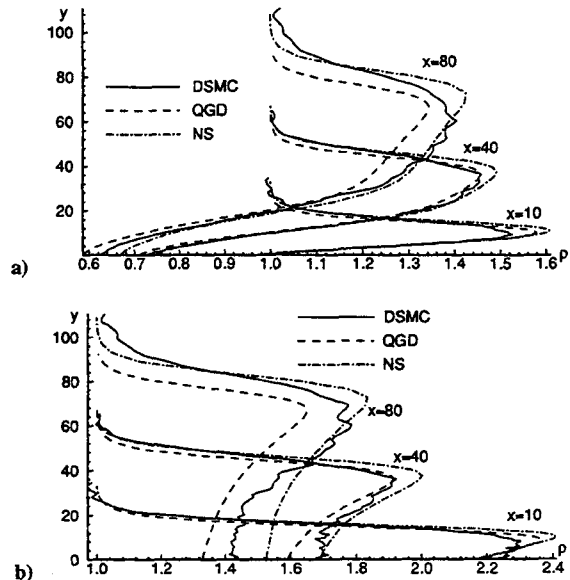


Fig. 10 $M_1 = 2$ and $T_w = T_0$: a) density profiles and b) pressure profiles.

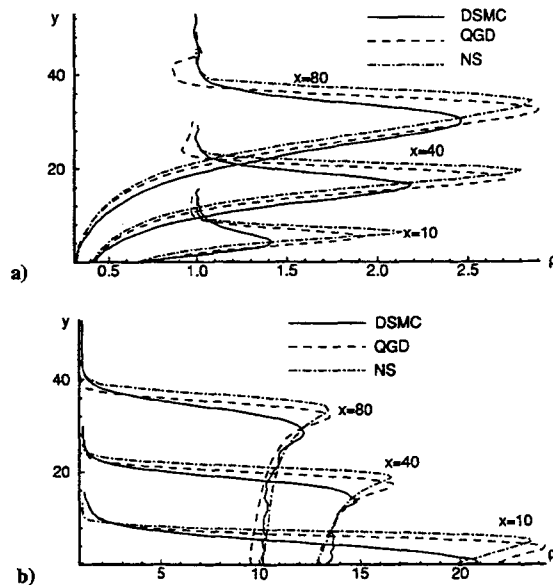


Fig. 11 $M_1 = 10$ and $T_w = T_0$: a) density profiles and b) pressure profiles.

$\bar{V}_{w,x} = M_1 \sqrt{C/Re_{w,x}}$, $\chi_{w,x} = \bar{V}_{w,x} M_1^2$, $M_1/\sqrt{Re_{w,x}}$ are derived by considering the viscosity at the wall temperature rather than in the freestream.

The values of these parameters are given in Table 2 for x taken from the $C_f/2$ distributions (Figs. 2–9). Based on Table 2, the breakdown of continuum approaches is best correlated by the parameters $M_1/\sqrt{Re_x}$ and \bar{V}_x . They can be interpreted as Knudsen numbers based on the boundary-layer thickness, with different approximations for the influence of wall temperature. This is because the present problem is essentially a flat plate boundary-layer problem. This also suggests that the influence of T_w should be introduced empirically. The criterion

$$(M_1/\sqrt{Re_x}) \times (T_1/T_w)^{0.17} = K$$

was found successful with K ranging from 0.39 to 0.87. The abscissa x at $M_1 = 1.5$ and 2 is not well defined because the continuum approach is valid very near to the leading edge. If these results are excluded from the study, K is nearly constant and equal to 0.42 ± 0.03 . For $K \geq 0.42$, the continuum description becomes deficient.

Table 2 Breakdown of continuum models

| M_1 | $T_w = T_0$ | | | | | $T_w = T_1$ | | | | |
|---|----------------|------|------|------|-------|----------------|------|-------|-------|-------|
| | 1.5 | 2 | 5 | 10 | 20 | 1.5 | 2 | 5 | 10 | 20 |
| x/λ_1 | ≈ 1 | 2 | 7 | 10 | 12 | ≈ 2 | 3 | 15 | 40 | 60 |
| Kn_x | ≈ 1 | 0.5 | 0.14 | 0.1 | 0.083 | ≈ 0.5 | 0.33 | 0.067 | 0.025 | 0.017 |
| Re_x | ≈ 2.5 | 6.6 | 58 | 165 | 396 | ≈ 4.9 | 10 | 124 | 659 | 1978 |
| $Re_{w,x}$ | ≈ 1.89 | 4.3 | 18.9 | 28 | 34 | ≈ 4.9 | 10 | 124 | 659 | 1978 |
| \bar{V}_x | ≈ 0.86 | 0.66 | 0.41 | 0.35 | 0.33 | ≈ 0.66 | 0.61 | 0.37 | 0.26 | 0.22 |
| $\bar{V}_{w,x}$ | ≈ 0.99 | 0.82 | 0.72 | 0.86 | 1.11 | ≈ 0.66 | 0.61 | 0.37 | 0.26 | 0.22 |
| χ_x | ≈ 1.94 | 2.67 | 10.3 | 35 | 130 | ≈ 1.48 | 2.4 | 9.3 | 26 | 87 |
| $\chi_{w,x}$ | ≈ 2.2 | 3.3 | 18 | 86 | 444 | ≈ 1.48 | 2.4 | 9.3 | 26 | 87 |
| $M_1/\sqrt{Re_x}$ | ≈ 0.95 | 0.78 | 0.66 | 0.78 | 1 | ≈ 0.67 | 0.64 | 0.45 | 0.39 | 0.45 |
| $M_1/\sqrt{Re_{w,x}}$ | ≈ 1.1 | 0.96 | 1.15 | 1.89 | 3.4 | ≈ 0.67 | 0.64 | 0.45 | 0.39 | 0.45 |
| $\frac{M_1}{\sqrt{Re_x}} \left(\frac{T_1}{T_w}\right)^{0.17}$ | ≈ 0.87 | 0.67 | 0.45 | 0.43 | 0.44 | ≈ 0.67 | 0.64 | 0.45 | 0.39 | 0.45 |

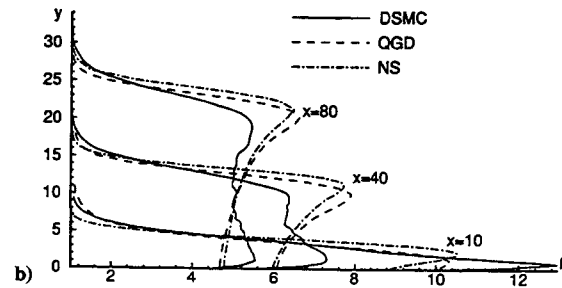
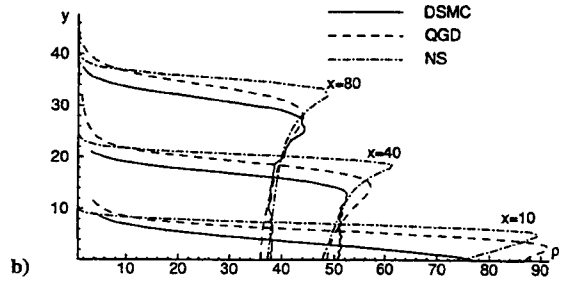
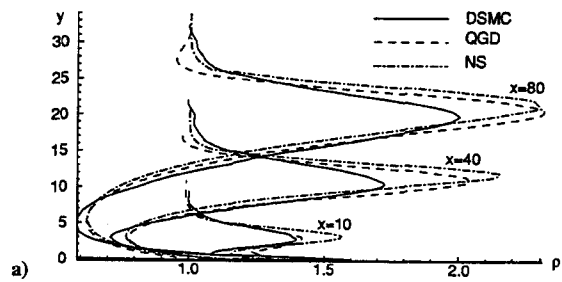
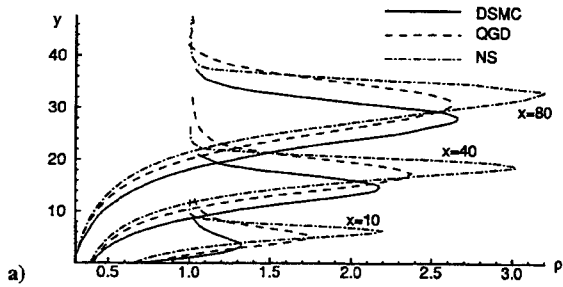


Fig. 12 $M_1 = 20$ and $T_w = T_0$: a) density profiles and b) pressure profiles.

Fig. 14 $M_1 = 10$ and $T_w = T_1$: a) density profiles and b) pressure profiles.

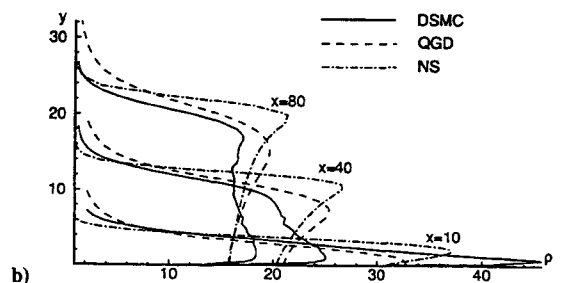
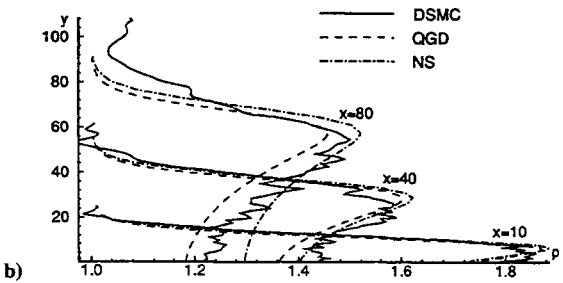
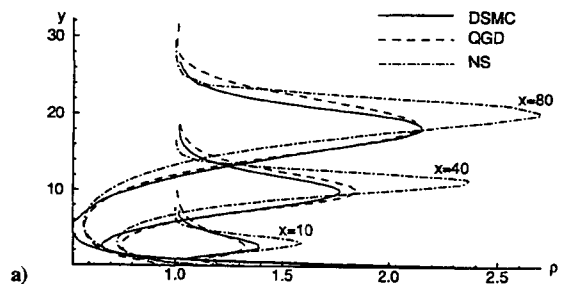
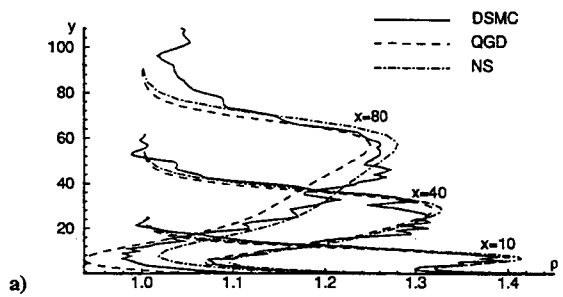


Fig. 13 $M_1 = 2$ and $T_w = T_1$: a) density profiles and b) pressure profiles.

Fig. 15 $M_1 = 20$ and $T_w = T_1$: a) density profiles and b) pressure profiles.

Conclusion

QGD equations have been introduced as a model for the description of viscous gas flows.

They are less sensitive than NS equations to computational instabilities induced by strong flow gradients.

The results support the proposed BCs for the QGD model, consisting of usual NS boundary conditions completed by an additional one requiring that pressure gradient normal to the wall be zero.

Based on comparisons with DSMC results, QGD equations give better results than NS for large values of M and Kn . Otherwise QGD and NS results tend to coincide. This suggests that the QGD equations are superior to the NS equations.

For small values of M , both continuum models are valid except in the immediate vicinity of the leading edge, as demonstrated by comparisons with DSMC results. A criterion has been proposed for the validity of the continuum approach in a wide range of Mach numbers and temperature ratios: it is recommended not to use a continuum approach when $(M_1/\sqrt{Re_x})(T_1/T_w)^{0.17}$ is larger than 0.42.

However, other configurations should be considered to give a more general character to these conclusions.

Acknowledgments

This research was supported by the Fund for Fundamental Investigations of the Russian Academy of Sciences N 94-01-01526. Discussions with B. Chetverushkin and the contribution of Y. Sheretov to the QGD correction procedure are gratefully acknowledged.

References

- ¹Bird, G. A., *Molecular Gas Dynamics and the Direct Simulation of Gas Flows*, Clarendon Press, Oxford, England, UK, 1994, Chaps. 7–11.
- ²Kogan, M. N., *Rarefied Gas Dynamics*, Nauka, Moscow, 1979, Chap. 5.
- ³Elizarova, T. G., and Chetverushkin, B. N., "One Numerical Algorithm for Simulation Gas Dynamic Flows," *Doklady Akademii Nauk SSSR*, Vol. 279, No. 1, 1984, pp. 80–83.
- ⁴Elizarova, T. G., and Chetverushkin, B. N., "Kinetically Coordinated Difference Schemes for Modelling Flows of a Viscous Heat-Conducting Gas," *Journal of Computational Mathematics and Mathematical Physics*, Vol. 28, No. 6, 1988, pp. 64–75.
- ⁵Abalakin, I. V., and Chetverushkin, B. N., "Using Kinetically-Consistent Difference Schemes for Prediction of Slightly Rarefied Gas Flows," *Journal of Mathematical Modelling*, Vol. 4, No. 11, 1992, pp. 19–35.
- ⁶Elizarova, T. G., and Sheretov, Y. V., "The Invariant Form and Asymptotic Properties of a Generalized Quasi-gas-dynamic System," *Journal of Computational Mathematics and Mathematical Physics*, Vol. 31, No. 7, 1991, pp. 72–78.
- ⁷Elizarova, T. G., Graur, I. A., and Sheretov, Y. V., "Quasi-gas Dynamic Equations and Computer Simulation of Rarefied Gas Flows," *Proceedings of the 19th International Symposium on Shock Waves at Marseille IV*, edited by R. Brun and L. Z. Dumitrescu, Springer-Verlag, 1995, pp. 45–50.
- ⁸Elizarova, T. G., and Gogolin, A. A., "Derivation of a Diffusion Term in Boltzmann Equation," *19th International Symposium on Rarefied Gas Dynamics*, edited by J. Harvey and G. Lord, Oxford Science Publications, Oxford, England, UK, Vol. 1, 1995, pp. 185–191.
- ⁹Elizarova, T. G., Graur, I. A., Lengrand, J. C., and Chpoun, A., "Rarefied Gas Flow Simulation Based on Quasi Gas Dynamic Equations," *Lab. d'Aérothermique du Center National de la Recherche Scientifique, RC 94-4*, Meudon, France, Aug. 1994.
- ¹⁰Schaaf, S. A., and Talbot, L., "Mechanics of Rarefied Gases," *Handbook of Supersonic Aerodynamics*, Sec. 16, Navy Dept., Bureau of Ordnance, NAVORD Rept. 1488, Washington, DC, Vol. 5, Feb. 1959.
- ¹¹Bird, G. A., "Definition of Mean Free Path for Real Gases," *Physics of Fluids*, Vol. 26, Nov. 1983, pp. 3222–3223.
- ¹²Lengrand, J. C., Chpoun, A., Allégre, J., Hériard-Dubreuilh, X., and Raffin, M., "Rarefied Hypersonic Flow over a Sharp Cone: DSMC, Navier-Stokes and Experimental Results," *Proceedings of the IUTAM Symposium on Aerothermochemistry of Spacecraft and Associated Hypersonic Flows*, edited by Brun and Chikhaoui, Univ. de Provence, Marseille, France, 1993, pp. 73–78.
- ¹³Skovorodko, P. A., and Lengrand, J. C., "Computation of Plume Flow Exhausting into a Vacuum, Including the Corresponding Viscous Flow in the Nozzle," *Lab. d'Aérothermique du Center National de la Recherche Scientifique, Meudon, France, R 90-9*, Dec. 1990.
- ¹⁴Anon., "INCA User's Manual," Amtec Engineering Inc., Bellevue, WA, 1993.
- ¹⁵Chpoun, A., Cohen, L., Lengrand, J. C., Allégre, J., and Raffin, M., "Numerical and Experimental Investigation of Rarefied Hypersonic Flow About a ASTV Re-Entry Body," *Computational Fluid Dynamics, Eccomas*, Wiley, New York, 1994, pp. 737–743.